8-26-2022

Global Modeling of Millimeter-Wave Transistors: Analysis of Electromagnetic-Wave Propagation Effects

Soheil Nouri
University of Arkansas, Fayetteville, sonouri@uark.edu

Samir M. El-Ghazaly
University of Arkansas, Fayetteville, elghazal@uark.edu

Citation

Nouri, S., & El-Ghazaly, S. M. (2022). Global Modeling of Millimeter-Wave Transistors: Analysis of Electromagnetic-Wave Propagation Effects. *IEEE Access, 10*, 92381-92389. https://doi.org/10.1109/ACCESS.2022.3201884

IEEE Access
Multidisciplinary | Rapid Review | Open Access Journal

Received 20 June 2022, accepted 23 August 2022, date of publication 26 August 2022, date of current version 8 September 2022.

Digital Object Identifier 10.1109/ACCESS.2022.3201884

RESEARCH ARTICLE

Global Modeling of Millimeter-Wave Transistors: Analysis of Electromagnetic-Wave Propagation Effects

SOHEIL NOURI, (Member, IEEE), AND SAMIR M. EL-GHAZALY, (Fellow, IEEE)
Department of Electrical Engineering, University of Arkansas, Fayetteville, AR 72701, USA

Corresponding author: Soheil Nouri (sonouri@uark.edu)

This work was supported by the University of Arkansas Libraries and the U.S. Army Research Office under Award W911NF-20-2-0120.

ABSTRACT In this study, the transmission line concept and the electron transport theory are consolidated in a global modeling approach, the wave-electron-transport (WET) model, to account for the physical phenomena in millimeter-wave devices. No equivalent circuit model is required to represent the innate properties of the device. Hence, the model is reliable for both small- and large-signal analyses. The electrodes of a transistor act as coupled multi-conductor transmission lines at millimeter-wave bands. The WET model consists of a device solver to obtain solutions for carrier-transport equations of the intrinsic device, and an electromagnetic solver (EM solver) to provide solutions for the governing transmission lines equations. As it is crucial to transfer data between these two solvers, an interface scheme is also developed and included in the WET model. The extrinsic parameters of the device are extracted using a novel systematic technique merely based on the physical structure of the transistor. In this paper, the modeling procedure is applied to a fabricated GaN-HEMT device. Power sweep analysis has verified the accuracy of the proposed model under both linear and non-linear operations. Non-uniform voltage distribution caused by traveling waves over the electrodes is elaborately discussed to demonstrate the necessity of incorporating distributed effects.

INDEX TERMS Electromagnetic-wave propagations, millimeter-wave transistor, non-linear operations, transmission line concept, wave-electron-transport model.

I. INTRODUCTION

The 5G wireless communication systems require high-speed transistors to process more data in a short time. High-frequency semiconductor devices are therefore in demand in 5G technologies for faster data communications. 5G base stations require power amplifiers with higher power density. Gallium nitride (GaN) is a wide bandgap semiconductor material that possesses high cut-off frequencies and high saturated electron velocity [1]. Silicon carbide and gallium arsenide-based device are being replaced by high electron mobility transistors (HEMTs) that utilizes GaN. The high power density and good thermal characteristics of GaN HEMTs make them preferable to build high power amplifiers [2]. The first step in the design of any high-frequency product is modeling. Fast simulation methods for modeling the carrier transport in semiconductors are presented in [3] and [4]. In a millimeter-wave band and for all applications, the size of the structure affects the performance and the wave propagations must be taken into account for modeling purposes [5]. The availability of a reliable simulation tool in a high-frequency design chain reduces the number of design cycles, shortens the design time, and reduces the design cost. High-frequency simulations based on empirical modeling may not be adequately accurate to cover all of the physical phenomena that impact high-frequency designs. Using experimental results in modeling requires data fitting and de-embedding the influence of pad parasitics and interconnect line effects. Measurement-based models are studied in [6], [7], [8], [9], and [10]. A comparison between three optimization techniques: Genetic Algorithm, Grey Wolf Optimization, and Harris-Hawks Optimization was studied in [6]. The test structure parasitics were modeled, and de-embedded, and the best match between measurements and

The associate editor coordinating the review of this manuscript and approving it for publication was Ladislau Matekovits.

models was shown up to 10 GHz. In [7], a compact model, electromagnetic simulation, and SPICE simulation method were presented. For parameter extraction, dc and s-parameter measurements are required and several parameters are fitted to a large number of data in this paper. Although this model may be consistent up to 40 GHz, it will be accurate only in the range of optimization. In [8], the Curtice model is used to fit the experimental results of the I-V characteristic to the parameters of a GaN HEMT device. Empirical models may provide accurate information about the fabricated device that is under investigation at a specific operating frequency range and bias conditions. However, they will be predictive neither for other functioning conditions of the same device nor other devices. Equivalent circuit models are the most common way of modeling millimeter-wave devices. In [9] and [10], efforts were made to account for the bias dependency of the extrinsic parameters. However, the accuracy of the models was not examined under non-linear operations. In [11], a physics-based model based on ASM-HEMT is proposed. An electromagnetic simulation is implemented to develop the distributed effects at Ka-band. A power amplifier measurement results are used to validate the model performance. However, the capability of the methodology was not examined for different device widths. Physics-based models are cheaper than conducting experiments. And they provide information that cannot be achieved by measurements. A physics-based modeling approach for electrical analysis of GaN HEMTs was proposed in [12]. The consistency of the approach is validated over a broad frequency range. This model needs to be modified in order to perform the large-signal analysis and take the effect of non-linearity into account [13]. In [14] a comprehensive physics-based model is proposed. In this paper, details of the modeling approach are presented. A novel parameter extraction methodology is included in the WET model, to obtain accurate values for the parasitic resistance of the electrodes. A new power sweep analysis incorporating the effects of skin depth on extrinsic resistance of electrodes is performed and the improved results are presented in this work. The generated results are compared with those of other models and the comparison confirms the accuracy of the modeling approach. The main contributions of this paper are:

1) Incorporating the wave-propagation effects in the proposed physics-based model for the first time; voltage waveforms over the electrodes of the millimeter device are simulated. The temporal and spatial distributions of the waveforms demonstrate the inevitable need to incorporate the electromagnetic-wave effects in the WET model.

2) Developing a novel parameter extraction methodology to improve the accuracy of the WET model at higher operating frequencies.

II. WET MODEL STRUCTURE

Fig. 1 depicts the general schematic of the millimeter-wave transistor defined in three-dimensional XYZ space together

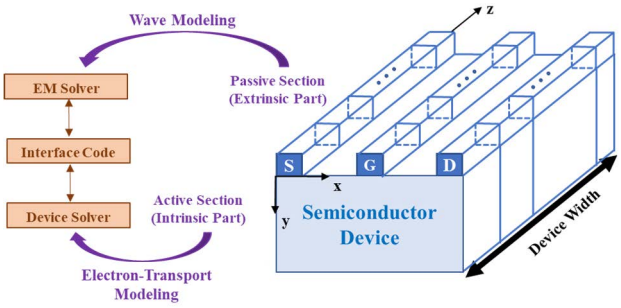

FIGURE 1. General schematic of a millimeter-wave transistor and WET model.

with the proposed model diagram. Intrinsic and extrinsic parts in this figure, represent the epitaxial layers and electrodes of the device that act as active and passive components in high-frequency operations, respectively. The transportation of carriers through the epitaxial layers is simulated in Silvaco Atlas software. This is accomplished by applying the associated differential equations derived from Maxwell's equations to the points in the two-dimensional grid of a device. The electrical performance of the device in the XY-plane is modeled by defining the physical geometry of the intrinsic part and feeding the bias conditions in the device solver. The hydrodynamic model is incorporated into the device solver to account for the effects of velocity overshoot, carrier temperature, and carrier energy distribution. Not all of the physical phenomena, however, take place in the intrinsic part. The z-dimension of the device, width, plays an important role in transistor functioning in millimeter-wave frequencies. Analyzing the device only in the XY plane would be adequate for electrically small devices where the device width is much smaller than the wavelength. As frequency increases, the device width becomes a considerable fraction of wavelength. Thus, the variability of the electrical waveforms along the electrodes' width, z-dimension, cannot be neglected. Hence, the electrical signal must be represented with spatial and temporal variations. The transmission line concept offers an accurate and computationally efficient approach to investigating this time- and space-variant system. To carry out the transmission line analysis, the per-unit-width parameters of the coupled multi-conductor lines are determined. Subsequently, the terminal conditions are applied according to the transistor pad layout [15]. The transmission line equations are then numerically solved by the EM solver that is shown in Fig. 1. The impact of electric currents that are injected from the intrinsic part into the electrodes must be incorporated into the EM solver.

Hence, the device solver should transfer this information about the intrinsic part to the EM solver. The EM solver should also provide the device solver with information about the bias points. Continuous data exchange is therefore a crucial task for the WET model. The interface code in Fig. 1 fulfills this duty.

III. PARAMETER EXTRACTION

Calculating the distributed capacitance needs solving a two-dimensional potential problem. The planar structure of the transistor makes it difficult to find a solution for the Laplace equation. In this work, a conformal mapping technique is utilized to map the boundaries of the planer structure into a simpler configuration for which the solution to the potential problem is easily found. Under this transformation, the coordinate system remains orthogonal to satisfy the Cauchy-Riemann condition. Consequently, the electrostatic energy and the characteristic of the medium formulated by permittivity, permeability, and conductivity remain unchanged. Although the geometry of the configuration is changed, the physical nature of the boundaries is identical in coordinate transformation. Thus the capacitance value is accurately calculated for the mapped configuration. To calculate the capacitance between every two plane electrodes, Schwarz-Christoffel mapping is utilized to map the whole space onto the interior of a parallel plate structure, assuming a zero thickness conductor. Then correction factors are determined based on Cohn's paper in [16] to compensate for the impact of metallization thickness. For the short-length millimeter-wave devices, the quasi-TEM mode is valid [17]. Therefore, to obtain the value of the inductance, it is assumed that the magnetic field is not affected by the presence of the epitaxial layers. Hence, with the unity dielectric constant, the inductance is derived from this equation:

$$\frac{1}{\sqrt{LC}} = c_0 \tag{1}$$

where L and C are per-unit-width inductance and capacitance of the electrodes respectively; and c_0 is the speed of the light in free space. To calculate the resistance per unit-width of the transmission line, a novel approach, representing an enhancement of Wheeler's incremental inductance rule [18], is developed. In Wheeler's method, the conductor loss is estimated with the assumption that the current distribution decreases gradually until it reaches zero, which requires a conductor thickness larger than 4 skin depths (δs). This assumption may not be always valid, depending upon the electrode thickness. To discuss the applicability (i.e., validity range) of Wheeler's method, three possible cases are anticipated in comparing the electrode's thickness (t) with the skin depth (δs) according to Fig. 2:

(a) $t < \delta s$
(b) $t > 4\delta s$
(c) $\delta s < t < 4\delta s$

In this figure, the current distribution is demonstrated for all three cases.

In case (a), the current distribution is uniform and the resistance is calculated using the following definition:

$$R = \frac{1}{\sigma(t.l)} \tag{2}$$

where R is per-unit-width resistance, σ is conductivity and l is the length of the conductor.

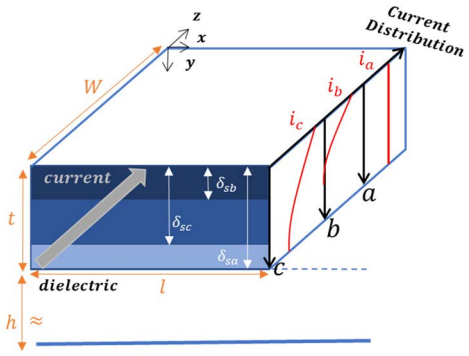

FIGURE 2. Skin depth and current distribution in conductors of millimeter-wave devices.

Case (b) represents the condition in which Wheeler's method is valid because the current density reaches zero at some point over the thickness. Hence, the whole conductor thickness does not contribute to the current conduction. For this case, the resistance is estimated based on the difference between the inductance of the original structure and another structure in which all sides of the conductor are recessed by δs/2. The resistance, in this case, is calculated using Eq. (3):

$$R = 2\pi f(L_\delta - L) \tag{3}$$

where f is the operating frequency, L is the inductance of the conductor and L_δ is the inductance after recessing the conductor surfaces by half of the skin depth.

In case (c), the current is distributed non-uniformly all over the thickness as it is depicted in Fig. 2. Hence, estimating the effective conductor's cross-sectional area becomes more involved. To obtain the resistance, the current distribution over the thickness is extracted based on the fact that the fields inside the conductor and the surface current density decay with depth exponentially [18]. In Fig. 2, for the sake of simple visualization, it is assumed that the magnetic field penetration takes place only from the upper side of the conductor (y=0). If the effect of skin depth is not taken into account, the value of resistance will be underestimated. And if Wheeler's method is not modified for the conditions described in case (c), the value of resistance will be overestimated.

An inaccurate value for the per-unit-width resistance will consequently affect the accuracy of the other simulated parameters such as cut-off frequency, output power, and gain. Eq. (3) is adjusted accordingly.

IV. NUMERICAL ANALYSIS

After extracting the per-unit-width parameters of the extrinsic part, the device width is divided into N segments. Considering dz to be the width of each segment the total device width (W) will be equal to:

$$W = N \times dz \tag{4}$$

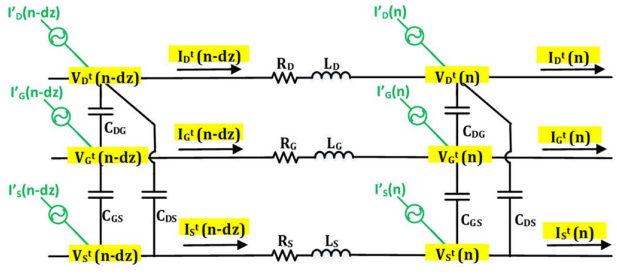

FIGURE 3. One unit segment of the WET model.

Fig. 3 illustrates the equivalent circuit of each unit segment that is a nominal T-configuration of a coupled transmission line.

The distributed effect is incorporated into the model by cascading these unit segments that form the total width of the device. R, L, and C are per-unit-width parameters of the coupled electrodes. Line voltages and currents noted by V and I are represented as traveling wave signals with temporal and spatial variations. As described in previous sections, the effect of intrinsic currents must be taken into account. For this purpose, the governing transmission line equations must be adjusted accordingly. The current sources that are identified by I'_d, I'_g, and I'_s in Fig. 3, represent the currents injected from the active layer into the drain, gate, and source lines. The transmission line equations associated with all electrodes are illustrated in (5-10). These equation sets are identical in form for all lines [19].

- Drain line equations:

$$R_D \frac{I_{D_n}^{t+dt} + I_{D_n}^{t}}{2} + L_D \frac{I_{D_n}^{t+dt} - I_{D_n}^{t}}{dt} = \frac{V_{D_n}^{t} - V_{D_{n+dz}}^{t}}{dz} \tag{5}$$

$$C_{DG} \frac{V_{DG_{n+dz}}^{t+dt} - V_{DG_{n+dz}}^{t}}{dt} + C_{DS} \frac{V_{DS_{n+dz}}^{t+dt} - V_{DS_{n+dz}}^{t}}{dt} = \frac{I_{D_n}^{t+dt} - I_{D_{n+dz}}^{t+dt} + I'^{t+dt}_{D_{n+dz}}}{dz} \tag{6}$$

- Gate line equations:

$$R_G \frac{I_{G_n}^{t+dt} + I_{G_n}^{t}}{2} + L_G \frac{I_{G_n}^{t+dt} - I_{G_n}^{t}}{dt} = \frac{V_{G_n}^{t} - V_{G_{n+dz}}^{t}}{dz} \tag{7}$$

$$C_{DG} \frac{V_{DG_{n+dz}}^{t+dt} - V_{DG_{n+dz}}^{t}}{dt} + C_{GS} \frac{V_{GS_{n+dz}}^{t+dt} - V_{GS_{n+dz}}^{t}}{dt} = \frac{I_{G_n}^{t+dt} - I_{G_{n+dz}}^{t+dt} + I'^{t+dt}_{G_{n+dz}}}{dz} \tag{8}$$

- Source line equations:

$$R_S \frac{I_{S_n}^{t+dt} + I_{S_n}^{t}}{2} + L_S \frac{I_{S_n}^{t+dt} - I_{S_n}^{t}}{dt} = \frac{V_{S_n}^{t} - V_{S_{n+dz}}^{t}}{dz} \tag{9}$$

$$C_{DS} \frac{V_{DS_{n+dz}}^{t+dt} - V_{DS_{n+dz}}^{t}}{dt} + C_{GS} \frac{V_{GS_{n+dz}}^{t+dt} - V_{GS_{n+dz}}^{t}}{dt} = \frac{I_{S_n}^{t+dt} - I_{S_{n+dz}}^{t+dt} + I'^{t+dt}_{S_{n+dz}}}{dz} \tag{10}$$

where the voltages on drain-gate (V_{DG}), drain-source (V_{DS}), and gate-source (V_{GS}) electrodes are:

$$V_{DG} = V_D - V_G \tag{11}$$

$$V_{DS} = V_D - V_s \tag{12}$$

$$V_{GS} = V_G - V_s \tag{13}$$

The superposition t represents the time and n denotes the spatial point. dt and dz are temporal and spatial step sizes, respectively. The value of dz is taken to be much smaller than the guided wavelength. This is to ensure that the value of the electric signal at each unit segment remains invariant. Otherwise, the KVL and KCL would fail to accurately describe the behavior of the device at each unit segment. The value of dt must be small enough to limit the numerical errors of the scheme and satisfy the Courant stability condition. Equations (5-10) are coupled equations and cannot be solved analytically. Hence, a numerical scheme is utilized to provide the solution for these equations. In this numerical analysis, equations (5), (7), and (9) are used to update the line currents, and equations (6), (8), and (10) update the line voltages. The EM solver accounts for the effect of the intrinsic part by including the injected currents from the epitaxial layers to (6), (8), and (10). And the device solver is fed with the values of the line voltages at every iteration of the numerical scheme.

V. SIMULATION RESULTS AND DISCUSSION

A. POWER SWEEP ANALYSIS

The proposed modeling scheme applied in this research work was validated in [14]. This was achieved by applying the proposed WET model to the fabricated GaN-HEMT device in [20]. Fig. 4, illustrates the device epitaxial structure and the comparison results. This N-polar device was grown on a SiC substrate.

The gate length is 0.1 μm and the device width is 2 $\times$ 25 μm. Gate has a mushroom shape to avoid high parasitic resistance and the stem height is 250 nm. The pad layout has a T-feed configuration. Gate and drain are the input and output lines, respectively. The device is biased at 12 V and 500 mA/mm under class-AB operations and a sinusoidal voltage is applied to the gate pad at 94 GHz. This voltage is increased gradually to sweep the power up to 20 dBm. The results presented in Fig. 4(b) and 4(c) demonstrate the enhancement of the new modeling scheme compared to that used in [14]. This enhancement is primarily due to the proposed parameter extraction method presented in Sec. III. of this paper.

As discussed before, any assumption about the current distribution of the conductors impacts the value of the resistances. And if the effect of skin depth in high frequency is not taken into account, the values obtained for resistance would

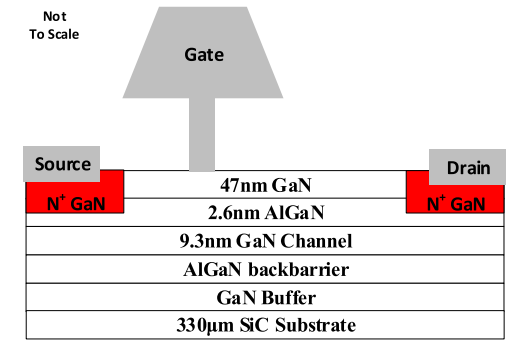

(a)

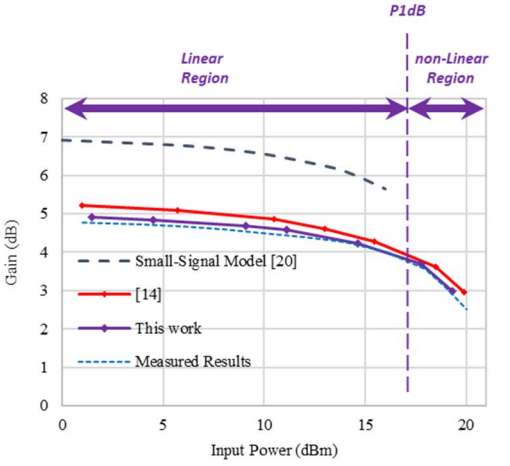

(b)

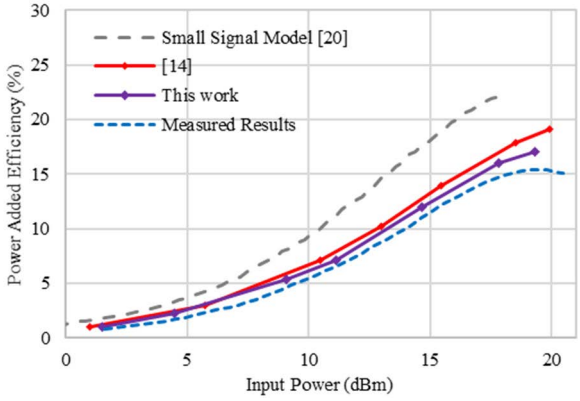

(c)

FIGURE 4. (a) Fabricated GaN-HEMT device in [20] (b) Gain comparison results (c) Power added efficiency comparison results.

TABLE 1. Per-unit-width resistance values.

	[14]	This work
R_D (Ω/cm)	98.7	118.4
R_G (Ω/cm)	167.8	187.1
R_S (Ω/cm)	98.7	111.6

not be sufficiently accurate. Table 1 compares the value of per-unit-width resistance obtained in this work with those used in [14].

Modified Wheeler's method gives a better estimation for the resistance since the thickness of the device is equal to $1.15\delta_s$ at 94 GHz. In [14], the current distribution was approximated to be uniform since the skin depth was believed to be roughly equal to the thickness of the conductors. This underestimates the resistance value which translates into a higher gain in [14] compared to the generated results in this work. This discrepancy is shown in Fig. 4(b) and 4(c). Under small-signal operations, output power increases linearly and the gain remains almost constant. As input voltage increases, the output power starts to saturate and there comes a point where the large-signal phenomenon is recognizable. As it is depicted in Fig. 4(b), the device reaches its 1 dB compression point (P1dB) at which the input power is about 17 dBm. Fig. 4(b) and 4(c) illustrate that the improved model used in this work offers more accurate results than the small-signal model in [14] during linear and non-linear operations. As expected, the small-signal model over-estimates the device behavior because of the following reasons:

- The model relies on measurement data. Thus, it includes the parasitic effects of device pads and interconnects that are not de-embedded.
- The model uses small-signal equivalent-circuit elements, and may not adequately account for the bias dependency of the intrinsic parameters. In large-signal operations, these variations appear to be significant and need to be accounted for.

B. WAVE PROPAGATION ANALYSIS

To further investigate the versatility of the presented model, the effect of electromagnetic wave propagations on the performance of millimeter-wave devices is studied. This is accomplished by employing this model to predict the performance of the fabricated MIS-HEMT device presented in [21]. The structure of the device is shown in Fig. 5. After fabrication, the two-dimensional electron gas density and average mobility of 1.1×10^{13} cm^{-2} and 1097 cm^2/(V.s) were recorded respectively by Hall measurements. The gate-source distance is 0.3 μm and the gate-drain spacing is 1.61 μm which is large enough to limit the drain-gate coupling and

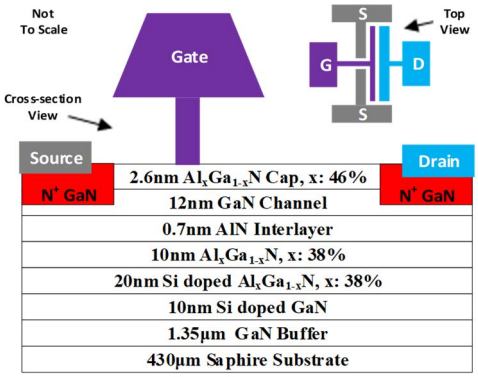

FIGURE 5. Fabricated GaN-HEMT device in [21].

the feedback capacitance. The gate length is 90 nm and the device width is 2 × 75 μm. Power sweep analysis of this device at 10 GHz was studied in [20].

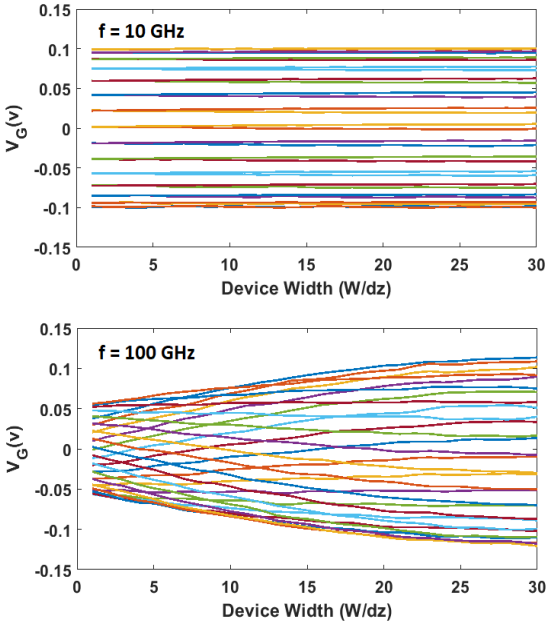

FIGURE 6. Time and space dependency of input line (gate electrode) voltage.

Fig. 6 shows the pattern of voltage waveforms along the input electrode at frequencies of 10 GHz and 100 GHz. To demonstrate the wave propagations over the electrodes, the voltage distribution at different time intervals is obtained and plotted. This graph presents the temporal and spatial evolution of the input voltage waveforms, simultaneously. This demonstrates that the electric size of the gate increases at higher frequencies and the distributed effects become more considerable.

To obtain the voltage distribution, the device width is divided into 30 segments. Each unit segment has a width (dz) of 2.5 μm. This dz is set to be much smaller than the guided wavelength. The pad layout of this device has a T-feed configuration with two fingers as outlined in the top view of the device in Fig. 5. The simulation has been conducted only for one finger and to account for the second finger appropriate boundary condition is implemented considering the symmetry of the configuration [15].

Fig. 7 illustrates the RMS values of the voltage distribution over input and output electrodes for six different operating frequencies, from 10 GHz to 60 GHz.

There are two observations in Fig. 7:

1. As presented in Fig. 7(a), the gate voltage is not distributed uniformly along the input electrode for frequencies higher than 10 GHz. The non-uniform drain voltage is also demonstrated in Fig. 7 (b). This effect is due to the presence of traveling waves on input and output electrodes at higher frequencies where the device width is comparable to the wavelength.

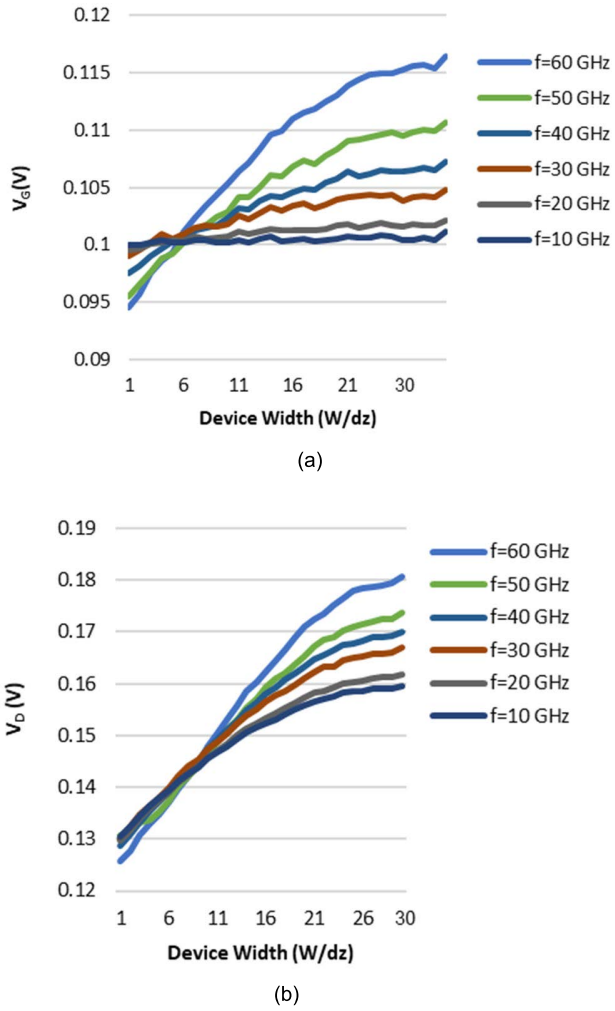

FIGURE 7. Voltage distribution along (a) Input line (gate electrode) and (b) output line (drain electrode).

As frequency increases the electrical width (not the physical width) of the electrodes increases and a more phase change is observed in the voltage waveforms over the electrodes. Hence, electromagnetic waves are the source of nonuniformity in signal electric properties (i.e. voltages and currents). Therefore, these variables must be characterized as spatial and temporal variations in millimeter-wave bands.

2. For all operating frequencies, the output transmission line (electrode) exhibits a more phase change than that of the input line. At 10 GHz, for instance, the gate voltage is uniform all along the electrode, but the drain electrode exhibits more presence of the traveling waves. This takes place because the drain electrode is a larger fraction of the wavelength. Hence, the drain is electrically wider than the gate and exhibits a more phase change. This is due to a phase velocity mismatch caused by their naturally different reactance. This phenomenon causes a partial phase-mismatch at W-band and beyond that significantly degrades the device performance.

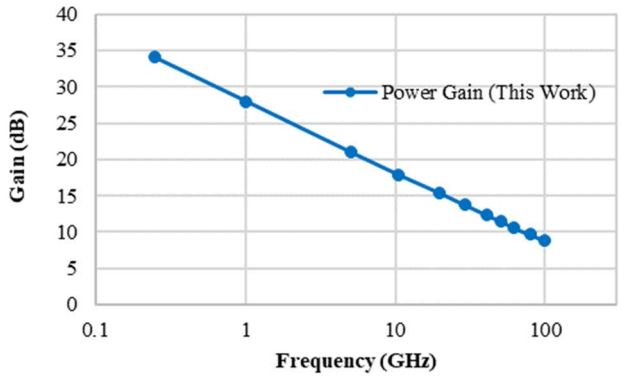

FIGURE 8. Power gain of the GaN-HEMT device offered by the WET model.

Fig. 8 presents the simulated power gain of the device versus frequency. The input and output lines are matched to the circuit in order to transfer the maximum energy. As frequency increases, the performance of the device is degraded as expected. The frequency response of the device is provided to show the ability of the modeling approach in predicting the device behavior in a broad frequency range. To obtain the power gain at each frequency, the equations (5)-(10) are solved after temporal and spatial discretization. In this scheme, equations (6), (8), and (10) are solved simultaneously to obtain the line voltages at all segments. These equations use (a) the previous time step values of line voltages; (b) the current time step value of intrinsic semiconductor currents updated by the device solver; and (c) the current time step value of line currents provided by equations (5), (7), and (9). And equations (5), (7), and (9) are also solved simultaneously to obtain the line currents at all segments.

These equations use: (a) the previous time step values of line currents; (b) the current time step value of line voltages provided by equations (6), (8), and (10). Using the value of voltages and currents at pad terminals, output power, input power, and gain are then calculated for each frequency.

C. INTERMODULATION ANALYSIS

The intermodulation distortion is one of the important metrics in analyzing the linearity of the RF and microwave components. At the device level, however, there is not much research available in the literature on multi-tone simulations.

In order to further evaluate the large-signal capabilities of the proposed modeling strategy, two-tone simulations are performed for two particular device structures in [22] and [23], and comparison results with measurements are presented in Fig. 9 (a).

The device structure in [22] is grown on Sapphire and is similar to the fabricated device in [21]. The only difference is GaN channel thickness and Al composition of the barrier which are changed to 9.3 nm and %27 respectively. The 3rd order intermodulation (IMD3) and the output third-order intercept point (OIP3) are obtained at two different bias points for a two-tone power sweep at 10 GHz with a tone spacing

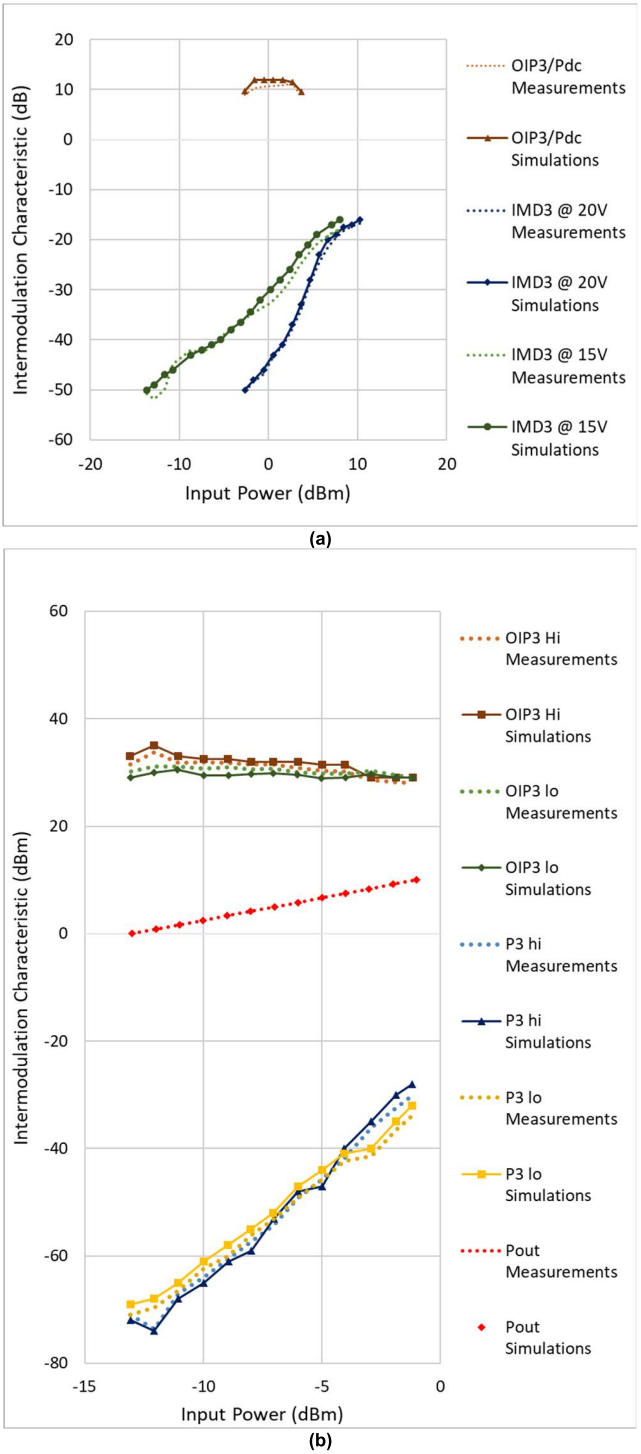

FIGURE 9. Two-tone power sweep simulation results compared to measurement results in (a) [22] (b) [23].

of 10 MHz. The WET model accurately predicts intermodulation distortion caused by non-linearity according to Fig. 9 (a). The measurement results in this figure are presented in [22] and the simulation results are based on the proposed modeling strategy in this work.

The device structure in [23] is grown on SiC and is similar to the fabricated device in [20]. The gate-source spacing

is 85 nm, the gate length is 60 nm and the gate-drain spacing is 315 nm. The simulation results offered by the WET model are compared to the measurement results presented in [23] and the results are shown in Fig. 9 (b). The fundamental output power, the upper and lower intermodulation products, and their associated OIP3 at 30 GHz with a tone spacing of 1 MHz are shown in this figure. The accuracy of the comparison results validates the consistency of the WET model. Since the proposed model in this work is physics-based, it is possible to optimize the device structure for low distortions.

The two-tone simulation results are also obtained for the device fabricated in [24]. The device is grown on a 400 μm SiC substrate. The transistor has four fingers; each finger width and length are 50 μm and 0.15 μm respectively. The gate-source spacing is 1 μm and the gate-drain spacing is 2.85 μm.

Figure 10 shows the fundamental, second, and third-order intermodulation power products. The simulation results in this graph are offered by the proposed model in this work and measurement results are obtained from [25]. This figure demonstrates that the WET model results are in very close agreement with the measurement results.

Table 2, summarize the comparison results presented in section V by providing the deviation from measurement results for each parameter in the proposed models in the literature. Not all references in Table 2 provided the simulation results for multi-tone intermodulation distortion. According to this table, the proposed WET model offers a lower deviation from measurement results. Hence, it provides a better prediction of the device behavior under non-linear operations.

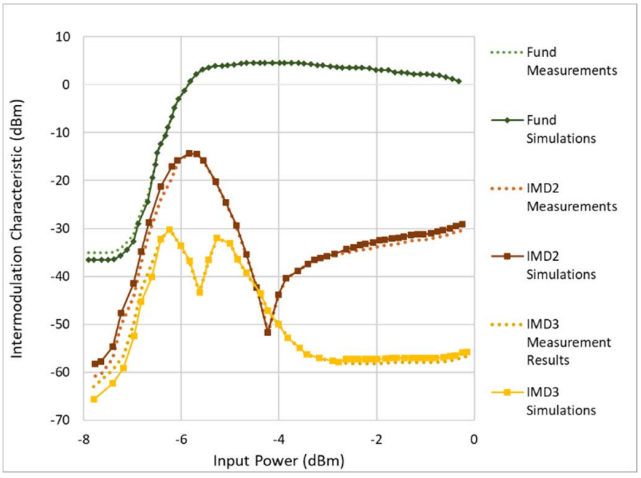

FIGURE 10. Two-tone power sweep simulation results compared to measurement results in [25].

TABLE 2. Performance of WET model in comparison with other references.

Deviation From Measurement Results		Single Tone Gain	Two-Tone Pout	Two-Tone IMD2	Two-Tone IMD3
[20]	Simulation [20]	2.2 dB	-	-	-
	This work	**0.1 dB**	-	-	-
[22]	Simulation [22]	-	-	-	-
	This work	**0 dB**	**0.2 dBm**	-	**0.9 dBm**
[23]	Simulation [23]	-	-	-	-
	This work	**0 dB**	**0 dBm**	-	**0.8 dBm**
[25]	Simulation [25]	-	2.4 dBm	2.9 dBm	3.1 dBm
	This work	-	**0.6 dBm**	**0.8 dBm**	**0.7 dBm**

VI. CONCLUSION

In this research work, a novel physics-based model for millimeter-wave transistors is presented. This model integrates the transmission line theory with the carrier transport properties of the device to account for the traveling waves. A novel parameter extraction method is proposed to find the parasitic resistance of the electrodes. Power sweep analysis is conducted to evaluate the performance of the modeling scheme in both linear and non-linear regions around the 1dB compression point. The WET model does not require any measurement data or equivalent circuit model to perform the analysis. The influence of traveling waves on the device is demonstrated by performing the wave propagation analysis. The WET model is comprehensive since it is predictive within the frequency range, bias conditions, and device-width it is intended for. This modeling approach provides insight into physical phenomena in the millimeter-wave band and is capable of being used as a simulation tool to design and optimize high-frequency devices.

ACKNOWLEDGMENT

This work was supported by the U.S. Army Research Office under Award W911NF-20-2-0120. Any opinions, findings, conclusions, or recommendations expressed in this paper are those of the authors and do not necessarily reflect those of the US Army Research Office. The authors would like to thank the University of Arkansas Libraries for supporting the publication of the paper in this journal.

REFERENCES

[1] A. Singh, S. K. Sinha, and S. Chander, "Analytical model of heterojunction tunnel field effect transistor incorporating the negative capacitance phenomenon," in *Proc. Int. Conf. Electron. Renew. Syst. (ICEARS)*, 2022, pp. 116–120, doi: 10.1109/ICEARS53579.2022.9751842.

[2] R. Ye, X. Cai, C. Du, H. Liu, Y. Zhang, X. Duan, and J. Zhu, "An overview on analyses and suppression methods of trapping effects in AlGaN/GaN HEMTs," *IEEE Access*, vol. 10, pp. 21759–21773, 2022, doi: 10.1109/ACCESS.2021.3139443.

[3] I. Harrysson Rodrigues and A. Vorobiev, "Low-field mobility and high-field velocity of charge carriers in InGaAs/InP high-electron-mobility transistors," *IEEE Trans. Electron Devices*, vol. 69, no. 4, pp. 1786–1791, Apr. 2022, doi: 10.1109/TED.2022.3147733.

[4] J. Cui, F. Feng, Z. Zhao, W. Liu, W. Na, and Q.-J. Zhang, "Recent advances in space mapping technique modeling GaN HEMT," in *Proc. 14th U.K.-Eur.-China Workshop Millimetre-Waves Terahertz Technol. (UCMMT)*, 2021, pp. 1–3, doi: 10.1109/UCMMT53364.2021.9569884.

[5] A. Shariffar, T. Bowman, C. Lai, M. Huang, M. El-Shenawee, and K. Bailey, "Modelling the interaction of THz waves with breast cancer tissues," in *Proc. IEEE Int. Symp. Antennas Propag. USNC/URSI Nat. Radio Sci. Meeting*, Jul. 2018, pp. 1843–1844.

[6] A. Abushawish and A. Jarndal, "Comparison of GA, GWO, and HHO optimization techniques for modeling substrate/buffer loading effect on GaN HEMTs," in *Proc. 14th Int. Conf. Develop. eSystems Eng. (DeSE)*, 2021, pp. 376–381, doi: 10.1109/DeSE54285.2021.9719328.

[7] S. Fregonese, M. Cabbia, C. Yadav, M. Deng, S. R. Panda, M. De Matos, D. Céli, A. Chakravorty, and T. Zimmer, "Analysis of high-frequency measurement of transistors along with electromagnetic and SPICE cosimulation," *IEEE Trans. Electron Devices*, vol. 67, no. 11, pp. 4770–4776, Nov. 2020, doi: 10.1109/TED.2020.3022603.

[8] S. Islam, M. A. Alim, A. Tahsin, F. R. Rakib, R. U. Rafi, and C. Gaquiere, "Performance projection of GaN HEMT: Experimental verification using curtice model," in *Proc. Int. Conf. Electron., Commun. Inf. Technol. (ICECIT)*, 2021, pp. 1–4, doi: 10.1109/ICECIT54077.2021.9641374.

[9] A. U. H. Pampori, S. A. Ahsan, R. Dangi, U. Goyal, S. K. Tomar, M. Mishra, and Y. S. Chauhan, "Modeling of bias-dependent effective velocity and its impact on saturation transconductance in AlGaN/GaN HEMTs," *IEEE Trans. Electron Devices*, vol. 68, no. 7, pp. 3302–3307, Jul. 2021, doi: 10.1109/TED.2021.3078717.

[10] A. Khusro, S. Husain, M. S. Hashmi, A. Q. Ansari, and S. Arzykulov, "A generic and efficient globalized kernel mapping-based small-signal behavioral modeling for GaN HEMT," *IEEE Access*, vol. 8, pp. 195046–195061, 2020, doi: 10.1109/ACCESS.2020.3033788.

[11] J. Hodges, S. A. Albahrani, B. Schwitter, and S. Khandelwal, "Accurate non-linear large signal physics-based modeling for Ka-band GaN power amplifier design with ASM-HEMT," in *IEEE MTT-S Int. Microw. Symp. Dig.*, Jun. 2021, pp. 349–351, doi: 10.1109/IMS19712.2021.9574979.

[12] A. G. Avval, S. Nouri, and S. M. El-Ghazaly, "Enhancing high-frequency performance of millimeter-wave transistors by optimizing device width," in *Proc. IEEE Texas Symp. Wireless Microw. Circuits Syst. (WMCS)*, 2022, pp. 1–4, doi: 10.1109/WMCS55582.2022.9866276.

[13] A. G. Avval, S. Nouri, and S. M. El-Ghazaly, "Effects of electromagnetic wave propagations in large-signal analysis of millimeter-wave transistors," in *Proc. IEEE 21st Annual Wireless Microw. Technol. Conf. (WAMICON)*, Apr. 2021, pp. 1–4, doi: 10.1109/WAMICON47156.2021.9443611.

[14] S. Nouri and S. M. El-Ghazaly, "Comprehensive physics-based model for millimeterwave transistors," in *Proc. IEEE Radio Wireless Symp. (RWS)*, Jan. 2021, pp. 29–31, doi: 10.1109/RWS50353.2021.9360354.

[15] S. Nouri, A. Ghadimi Avval, and S. M. El-Ghazaly, "Effects of pad layout variations on the cut-off frequency of millimeter-wave transistors," in *Proc. IEEE Texas Symp. Wireless Microw. Circuits Syst. (WMCS)*, May 2021, pp. 1–4, doi: 10.1109/WMCS52222.2021.9493270.

[16] I. Erdin and R. Achar, "Modeling of asymmetric differential striplines including crossing junction discontinuities," *IEEE Trans. Electromagn. Compat.*, vol. 60, no. 1, pp. 50–58, Feb. 2018, doi: 10.1109/TEMC.2017.2726996.

[17] S. M. El-Ghazaly and T. Itoh, "Traveling-wave inverted-gate field-effect transistors: Concept, analysis, and potential," *IEEE Trans. Microw. Theory Techn.*, vol. 37, no. 6, pp. 1027–1032, Jun. 1989, doi: 10.1109/22.25407.

[18] S. Ahyoune, J. Sieiro, M. N. Vidal, and J. M. López-Villegas, "Skin effect formula for metal strips in laminated substrates," in *Proc. 32nd Conf. Design Circuits Integr. Syst. (DCIS)*, 2017, pp. 1–4, doi: 10.1109/DCIS.2017.8311642.

[19] S. Nouri, A. G. Avval, and S. M. El-Ghazaly, "Impact of wave propagations on figures of merit in millimeter-wave transistors," in *IEEE MTT-S Int. Microw. Symp. Dig.*, Jun. 2021, pp. 352–354, doi: 10.1109/IMS19712.2021.9574880.

[20] M. Guidry, S. Wienecke, B. Romanczyk, H. Li, X. Zheng, E. Ahmadi, K. Hestroffer, S. Keller, and U. K. Mishra, "Small-signal model extraction of mm-Wave N-polar GaN MISHEMT exhibiting record performance: Analysis of gain and validation by 94 GHz loadpull," in *IEEE MTT-S Int. Microw. Symp. Dig.*, May 2016, pp. 1–4.

[21] X. Zheng, H. Li, S. Wienecke, B. Romanczyk, K. Hestroffer, E. Ahmadi, M. Guidry, S. Keller, and U. K. Mishra, "High frequency N-polar GaN planar MIS-HEMTs on sapphire with high breakdown and low dispersion," in *Proc. Lester Eastman Conf. (LEC)*, Bethlehem, PA, USA, 2016, pp. 42–45.

[22] A. Arias, P. Rowell, J. Bergman, M. Urteaga, K. Shinohara, X. Zheng, H. Li, B. Romanczyk, M. Guidry, S. Wienecke, E. Ahmadi, S. Keller, and U. Mishra, "High performance N-polar GaN HEMTs with OIP3/Pdc ~ 12dB at 10GHz," in *Proc. IEEE Compound Semicond. Integr. Circuit Symp. (CSICS)*, Oct. 2017, pp. 1–3, doi: 10.1109/CSICS.2017.8240456.

[23] P. Shrestha, M. Guidry, B. Romanczyk, N. Hatui, C. Wurm, A. Krishna, S. S. Pasayat, R. R. Karnaty, S. Keller, J. F. Buckwalter, and U. K. Mishra, "High linearity and high gain performance of N-polar GaN MIS-HEMT at 30 GHz," *IEEE Electron Devices Lett.*, vol. 41, no. 5, pp. 681–684, Mar. 2020, doi: 10.1109/LED.2020.2980841.

[24] M. A. Alim, A. A. Rezazadeh, and C. Gaquiere, "Temperature effect on DC and equivalent circuit parameters of 0.15- μm gate length GaN/SiC HEMT for microwave applications," *IEEE Trans. Microw. Theory Techn.*, vol. 64, no. 11, pp. 3483–3491, Nov. 2016, doi: 10.1109/TMTT.2016.2604815.

[25] M. A. Alim, M. M. Ali, A. A. Rezazadeh, and C. Gaquiere, "Temperature dependence of the Taylor series coefficients and intermodulation distortion characteristics of GaN HEMT," *IEEE Trans. Comput.-Aided Design Integr. Circuits Syst.*, vol. 39, no. 3, pp. 552–559, Mar. 2020, doi: 10.1109/TCAD.2019.2897696.

SOHEIL NOURI (Member, IEEE) received the M.Sc. degree in electrical engineering from the University of Arkansas, Fayetteville, AR, USA, where he is currently pursuing the Ph.D. degree in electrical engineering. His current research interests include semiconductor device simulations, numerical technologies applied to MMICs, and microwave and millimeter-wave devices and circuits. He was the winner of the First Best Student Paper Award, the three-minute thesis competition, and the research competition at the 2020 Mediterranean Microwave Symposium, 2021 IEEE MTT-S International Microwave Symposium, and 2022 IEEE Texas Microwave Symposium, respectively.

SAMIR M. EL-GHAZALY (Fellow, IEEE) received the Ph.D. degree in electrical engineering from The University of Texas at Austin, Austin, TX, USA, in 1988. He joined the Department of Electrical Engineering, Arizona State University, as an Assistant Professor, where he was an Associate Professor, in 1993, and a Professor, in 1998. From August 2002 to July 2007, he was the Head of the Department of Electrical and Computer Engineering, University of Tennessee, Knoxville, TN, USA. From August 2007 to June 2013, he was the Head of the Department of Electrical Engineering and the holder of the 21st Century Leadership Endowed Chair in electrical engineering with the University of Arkansas. He is currently a Distinguished Professor with the Department of Electrical Engineering, University of Arkansas. He has completed two detail assignments at the U.S. National Science Foundation (NSF): From August 2013 to August 2016, he was the Director of the Division of Electrical, Communications and Cyber Systems at NSF. This division supports research in advanced areas of critical importance for the U.S. economy and defense. From September 2009 to August 2012, he was the Program Director for electronics, photonics, and magnetic devices with the Division of Electrical, Communications and Cyber Systems. He trained and worked at several universities and research centers, including Cairo University; the Centre Hyperfrequences et Semiconducteurs, Université de Lille, France; the NASA's Jet Propulsion Laboratory, Pasadena, CA, USA; CST-Motorola, Inc.; iemn, the Université de Lille; and the Swiss Federal Research Institute (ETH). His research interests include microwave and millimeter-wave semiconductor devices and circuits, semiconductor device simulations, electromagnetics, antennas, and numerical techniques applied to monolithic microwave integrated circuits. He was an Elected Member of the Administrative Committee of the IEEE Microwave Theory and Techniques Society, from 2001 to 2013. He received the Distinguished Educator Award from the IEEE Microwave Theory and Techniques Society, in 2015. He was the General Chairman of the IEEE MTT-S International Microwave Symposium, Phoenix, Arizona, in May 2001. He was the Chairperson of the Commissions A and D of the U.S. National Committee of URSI, the MTT-15 Committee on Field Theory, and the IEEE MTT-S Publications Committee, from 2004 to 2008. He was the Chair of the Publication Services and Products Board, the IEEE Technical Activities Board's Periodicals Committee, from 2012 to 2013, and the IEEE-TAB Periodical Review and Advisory Committee, from 2014 to 2015. He was the President of the IEEE Microwave Theory and Techniques Society, in 2010. He was the Vice President of the Institute of Electrical and Computer Engineering (IEEE), in 2018 and 2019.